electronics

MDPI

Communication

Design of a High-Gain Hybrid Slot Antenna Array Based on Bulk Silicon MEMS Process for W-Band Applications

Yu Zhao [1], Hao Luo [2], Wenhao Tan [1], Zheng Zhou [1], Guoqiang Zhao [1,*] and Houjun Sun [1]

[1] School of Integrated Circuits and Electronics and the Beijing Key Laboratory of Millimeter Wave and Terahertz Technology, Beijing Institute of Technology, Beijing 100081, China; 3120170366@bit.edu.cn (Y.Z.); tanwenhao@bit.edu.cn (W.T.); 3120221374@bit.edu.cn (Z.Z.); sunhoujun@bit.edu.cn (H.S.)
[2] National Key Laboratory of Science and Technology on Test Physics & Numerical Mathematics, China Academy of Launch Vehicle Technology, Beijing 100071, China; 7520190142@bit.edu.cn
* Correspondence: zhaoguoqiang@bit.edu.cn

Abstract: A W-band, high-gain, hybrid slot antenna array based on bulk silicon MEMS technology is proposed in this paper. The high-order-mode cavity is explored to excite the 2 × 2-slot basic unit, so as to reach the low-profile requirement of the bulk silicon MEMS process. To avoid the fragile structure of the large-scale antenna arrays based on the bulk silicon MEMS process, the ridge gap waveguide is employed to build the feed network for a large-scale array. A vertical transition between a rectangular waveguide and a ridge gap waveguide is designed to support the low-loss and low-cost assembling method between the radiation units and the feed network. An 8 × 8-slot hybrid antenna array is simulated and fabricated. The measured results show a relative bandwidth (VSWR < 2) of 8.1% with the first side-lobe level less than −11 dB over the frequency band of 91–97 GHz. A maximum gain of 26.1 dBi with the radiation efficiency of 65.2% is achieved. With high gain and high fabrication efficiency, the proposed hybrid slot antenna array would be valuable for W-band radar applications.

Keywords: slot antenna array; high gain; hybrid array; bulk silicon MEMS; W-band

Citation: Zhao, Y.; Luo, H.; Tan, W.; Zhou, Z.; Zhao, G.; Sun, H. Design of a High-Gain Hybrid Slot Antenna Array Based on Bulk Silicon MEMS Process for W-Band Applications. *Electronics* **2023**, *12*, 2028. https://doi.org/10.3390/electronics12092028

Academic Editors: George Kyriacou and Constantinos L. Zekios

Received: 18 March 2023
Revised: 23 April 2023
Accepted: 24 April 2023
Published: 27 April 2023

1. Introduction

With the advantages of high detection accuracy, W-band radar systems have been used in auto-motive radars, blast furnace radars, and foreign object debris (FOD) radars [1–4]. In these applications, a high-gain and wide-band antenna array is helpful to achieve the high detection power and accuracy of the radar system. Furthermore, the low cost and high fabrication efficiency features must be considered during the antenna array design, so as to facilitate the batch production of these radar products.

The antenna array can be divided into the radiation part and the feed network; the overall performance of an antenna array is determined by the form and fabrication process of the two parts. The patch antenna is widely used in mm-wave antenna array design, due to its low profile and low-cost features [5–7]. However, dielectric loss at the mm-wave band will reduce the gain of the antenna array, especially when the array scale becomes large. The waveguide slot antenna arrays presented in [8–11] are based on the waveguides which have low transmission loss and feature high gain. However, their working bandwidths are narrow, as the slots are resonant units and are all series-feed. The slot antenna arrays in [12–15] utilized the air cavity and the corporate-feed network to realize the full corporate-feed of each radiation unit, a method which can achieve both the wide-band and high-gain features. However, these arrays are all based on laser etching and diffusion bonding processes, which have high fabrication costs.

The slot arrays based on a substrate-integrated waveguide (SIW) in [16–18] have the features of a low profile and low fabrication cost, but the dielectric loss at W-band will reduce the radiation efficiency of the antenna array. The low-loss, ridge gap waveguide

(RGWG) is adopted to build mm-wave band antenna arrays in [19–23]. Periodically distributed metal columns are used to build the artificial magnetic conductivity (AMC) boundary, so that the waveguide can be fabricated without an expensive bonding process. The RGWG-based antenna arrays in [19,20] have the advantage of high-gain and low fabrication cost, but the resonant radiation unit brings narrow working bandwidth. By combining high-gain and wide-band radiation units with RGWG feed networks, some hybrid arrays are presented in [21–23]. The LTCC-based, SIW-feed mixed with an RGWG feed network antenna array is proposed in [21,22]; the array has a wide-band and low profile but also has a low radiation efficiency. An ME dipole array with an RGWG feed network has been reported in [23]. A relative bandwidth of 13% with $|S_{11}| < -10$ dB and a gain higher than 18 dBi can be achieved. However, the co-axial feeding structure used in the radiation units is hard to fabricate at the W-band, and the fabrication accuracy of the multi-layer PCB process cannot reach the requirement at the W-band. The bulk silicon MEMS process has the advantages of high fabrication accuracy and high fabrication efficiency, which has been used in mm-wave band antenna design [24–26]. The slot array in [24] has a simple structure and high gain, but the resonant structure brings narrow bandwidth. The corporate-feed horn arrays in [25,26] have both the high-gain and wide-band features. However, with the feature of fragility, the scale of the antenna array based on the bulk silicon MEMS process is limited.

In this paper, we propose a high-gain, hybrid slot antenna array with high fabrication efficiency for a W-band, large-scale array design. The bulk silicon MEMS technology is used to design the radiation unit. The high-order-mode cavity is explored to excite the 2×2-slot basic unit, so as to satisfy the low-profile requirement of the bulk silicon MEMS process. To avoid the fragility of the antenna based on the bulk silicon MEMS process as the array scale becomes large, the ridge gap waveguide is employed to build the feed network for a large-scale array. The total array can be fabricated via bulk silicon MEMS technology and CNC milling and assembled without an expensive bonding process. An 8×8-slot hybrid antenna array is simulated and fabricated. The measured results show a relative bandwidth (VSWR < 2) of 8.1% with the first side-lobe level less than -11 dB over the frequency band of 91–97 GHZ. The maximum gain of 26.1 dBi with the radiation efficiency of 65.2% is achieved. The measured results indicate that the proposed hybrid array has high-gain and high-efficiency features.

2. The 4×4-Slot Sub-Array Based on Bulk Silicon MEMS Process

2.1. Configuration and Operation Mechanism of the Basic Unit

The basic unit of the hybrid antenna array is a 2×2-slot sub-array, which is excited by the high-order-mode cavity. Figure 1a exhibits the configuration of the proposed 2×2-slot basic unit. The sub-array structure is constituted of five thin, laminated, metallic plates. On the top layer, four rectangular slots with the size of $w_s \times l_s$ are excited by the high-order-mode cavity on the second layer. In comparison with the cavities in [12], the cavity in this paper has a larger planar size but a lower section size, which is more suitable for the bulk silicon process. On the third layer, an offset longitude slot is used to couple the EM-wave from the rectangular waveguide (RWG) on the fourth layer to the cavity. The height of the RWG is reduced so that it can satisfy the thickness requirement of bulk silicon. A metal step with the size of $w_m \times l_m$ is placed on the waveguide wall opposite the offset slot to achieve good impedance matching at the feed port. These plates are 250 μm thick silicon wafers which are etched using the deep reactive ion etcher (DRIE) process, gold-plated, and bonded together with a diffusion bonding process.

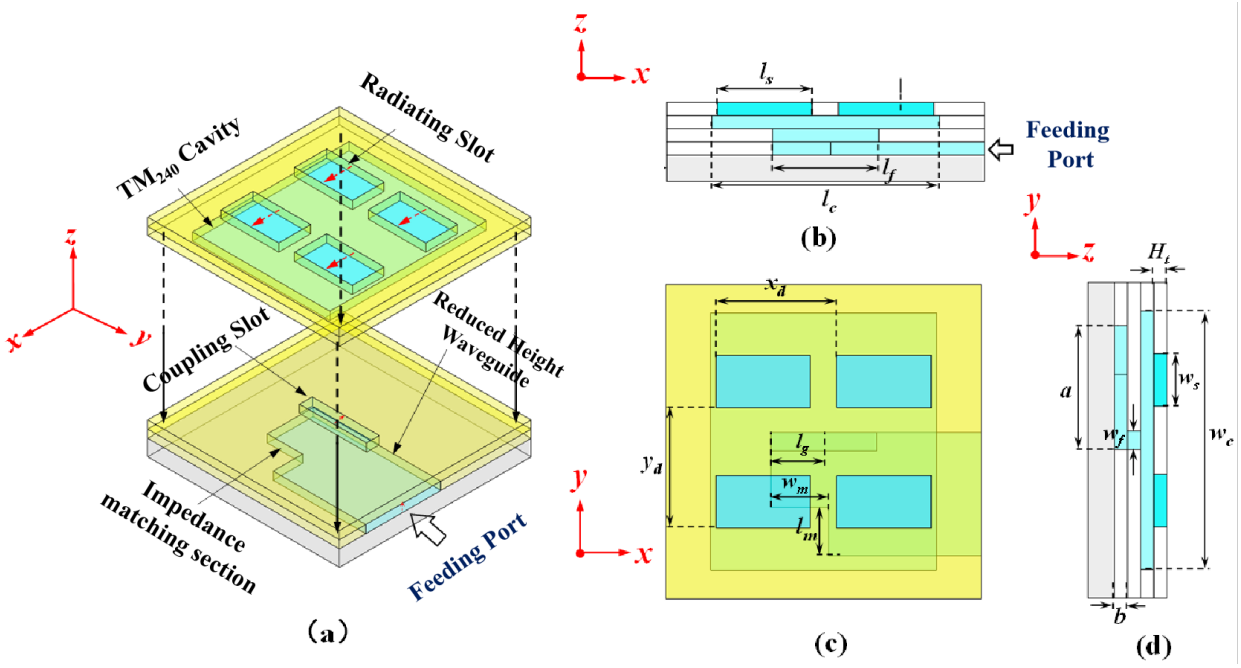

Figure 1. The 2 × 2-slot basic unit. (**a**) Isometric view. (**b**) Front view. (**c**) Top view. (**d**) Left view.

Figure 2 illustrates the electric and magnetic field distribution of the sub-array. The electric field distribution of the radiating aperture indicates the antenna radiates linearly polarized waves. The operation principle of the sub-array proposed in this paper is similar to the one in [12]. The *x*-direction magnetic current of the rectangular waveguide is cut by a coupling slot, and then it enters into the cavity and excites the TM_{240} mode. The magnetic field distribution in the cavity is symmetrical with the *x* axis. The four radiating slots are eventually placed at the appropriate position in the y-direction of the cavity, so that the magnetic current along the *x* direction can be intercepted to the greatest extent. The phase of the magnetic current in the cavity is opposite to the *y*-axis. Therefore, by placing the radiating slots on both sides of the *y*-axis symmetrically, the EM-waves radiated from the sub-array into free space have high polarization purity.

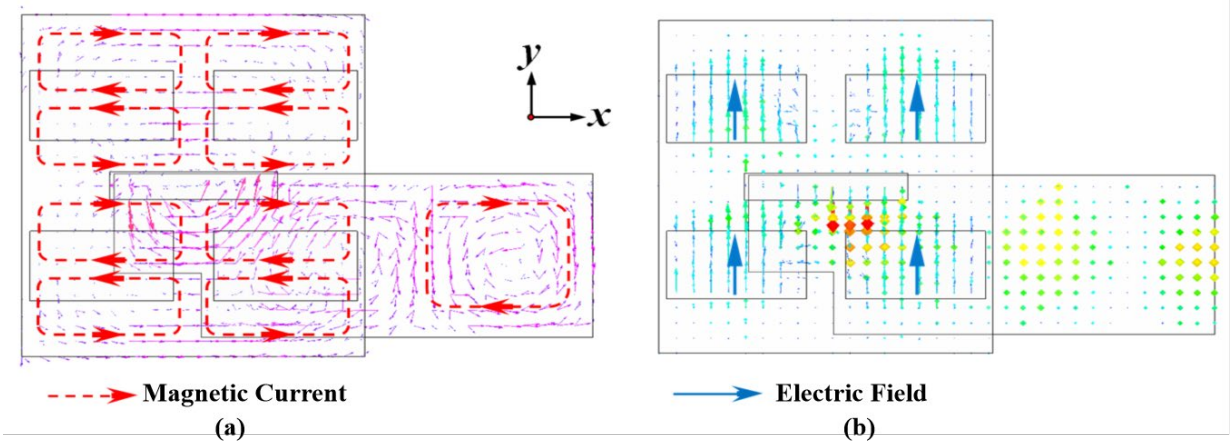

Figure 2. Magnetic current and E-field distribution of the 2 × 2-slot basic unit. (**a**) Magnetic current distribution. (**b**) Electric field distribution.

The main part of the 2 × 2-slot basic unit is the high-order-mode cavity, which can realize the compact profile of the corporate-feed waveguide slot antenna. Figure 3 exhibits the simulated electric field magnitude distributions in the cavity, which are simulated by

the electric magnetic simulation software ANSYS Electronics Desktop. Here, T represents a period of time, and it can be seen that when t = 0 and t = T/2, the dominant mode in the cavity is the TM_{240} mode. When t = T/4 and t = 3T/4, the TM_{240} mode is weaker than t = 0 and t = T/2. Although there are other modes, the field of the TM_{240} mode is still stronger, meaning that the cavity can still be regarded as operating in the TM_{240} mode.

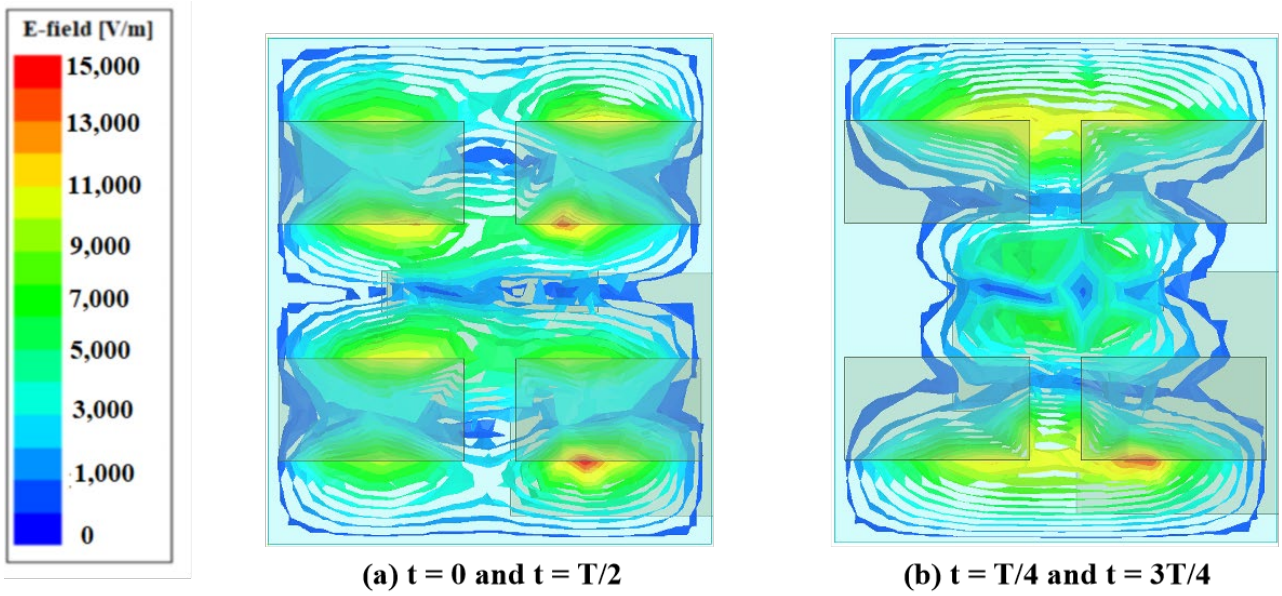

Figure 3. E-field distribution of the high-order-mode cavity in 2 × 2-slot basic unit while (**a**) t = 0 and t = T/2 (**b**) t = T/4 and t = 3T/4.

2.2. Parameter Analysis of the Basic Unit

The working mechanism of the high-order-mode excited 2 × 2-slot basic unit is discussed in the previous section. In this section, the key parameters will be studied to give the design guideline of the proposed slot antenna. According to the working mechanism, the high-order-mode cavity is the main part of the sub-array. In this application, the substrate is set as vacuum, and the thickness of the cavity is fixed to 0.25 mm under the bulk silicon background. The relationship between the dimension of the cavity and the frequency of the resonant mode can be summarized as follows:

$$f_{mnp} = \frac{1}{2\sqrt{\mu\varepsilon}}\sqrt{\left(\frac{m}{w_c}\right)^2 + \left(\frac{n}{l_c}\right)^2 + \left(\frac{p}{h_c}\right)^2} \quad (1)$$

where w_c, l_c, and h_c are the width, length, and height of the cavity. In order to make the cavity work in the TM_{240} mode, the initial values of w_c and l_c are set to $1.5\lambda_0$ and $1.2\lambda_0$; however, the specific values of length and width can be optimized nearby the initial values. Figure 4a,b show the changes in the S parameter when l_c and w_c take different values. It can be seen that when the length and width values increase, the S parameter of the sub-array has two obvious resonant points, which further expand the bandwidth of the antenna. The dual-resonant points originate from the interaction between the radiation slot and the free space when the TM_{240} mode is excited. On the other hand, it can be observed that with the further increase in length and width, the two resonant points gradually separate, and the S parameter curve also gradually rises, indicating that the impedance matching between the sub-array and the free space gradually becomes worse in this situation. Therefore, the length and the width of the cavity is optimized to 4.2 mm and 4.8 mm, respectively.

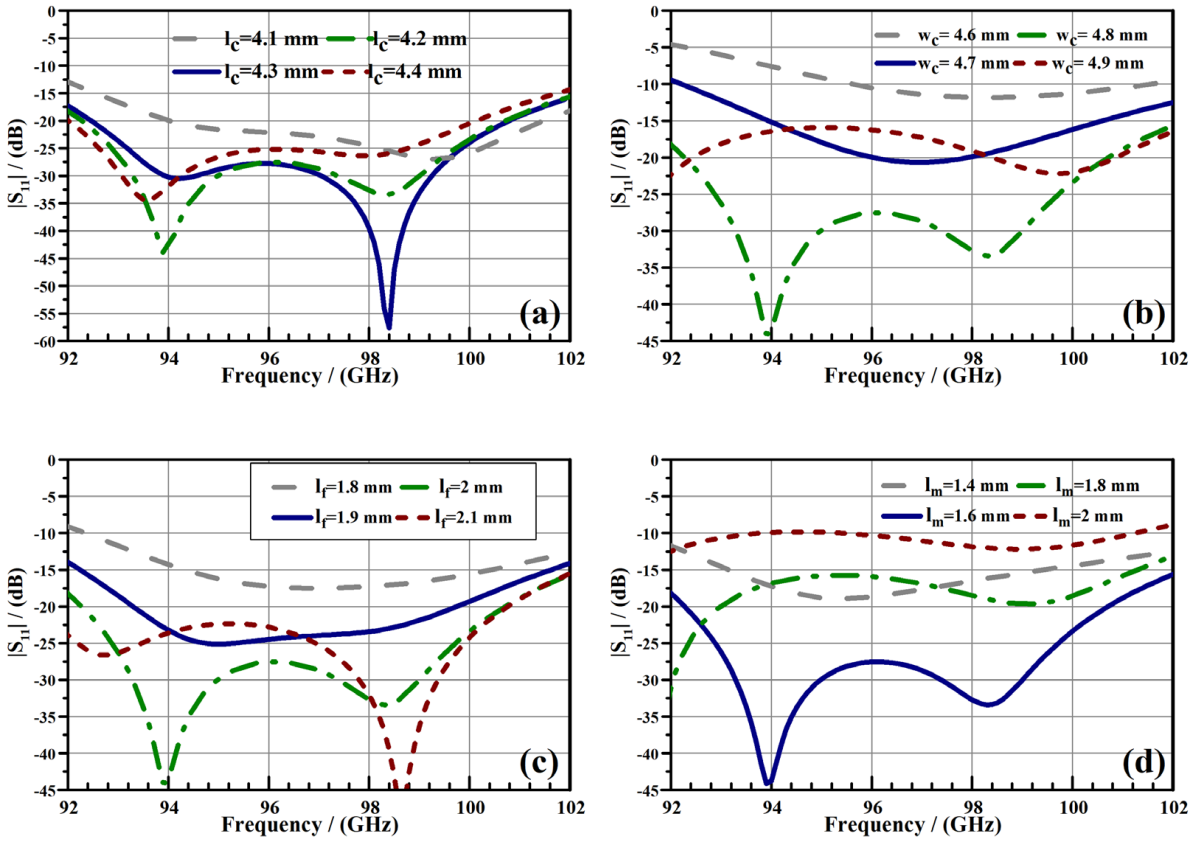

Figure 4. Parameter analysis of the feeding part. (**a**,**b**) Length and width of the cavity. (**c**) Length of the coupling slot. (**d**) Length of the impedance matching step.

The coupling slot is one of the key components. Its length affects the impedance matching between the cavity and the reduced height RWG. Figure 4c shows the change in the S parameter when the slot length is set from 1.8 mm to 2.1 mm. Two resonant points can also be observed for different S11 curves under different slot lengths, and the shorter the slot length is, the closer the resonant points are. Meanwhile, the longer the slot is, the greater the resonant point spacing is. At the same time, the parameter S will gradually rise, which is consistent with the influence trend of the length and width of the cavity. There is also an optimal solution, which is selected as l_f = 2 mm. In addition, the size of the impedance matching step on the short-end, reduced-height RWG also affects the feeding performance, especially the length *lm* of the step. Figure 4d shows the changes in the S parameter when different lm values are taken. It can be seen that the increase in l_m will increase the distance between the two resonant points. At the same time, with the rise in the S parameter, there is also an optimal solution, which is taken as 1.6 mm.

In the radiation part, the length and width of the radiating slot are determined by the working mode and size of the cavity. However, the distance between adjacent slots in the x and y directions has a greater impact on its radiation performance. Figure 5a,b show the E-plane and H-plane radiation patterns at different x- and y-direction distances. The results show that with increased slot spacing, the gain in the sub-array increases slightly, the main beam width gradually narrows, and the sidelobe level significantly rises. The slot spacing should be as small as possible, so that the low sidelobe can be realized. However, the slot spacing in the x- and y-direction also affects the feed performance of the sub-array. Figure 4c,d give the changes in the feed performance of the different slot spacing values. When considering the radiation and feed performance comprehensively, there is an optimal solution for the cell spacing value, which is 2.4 mm and 2.2 mm, respectively. The final dimensions of the 2 × 2-slot sub-array are shown in Table 1.

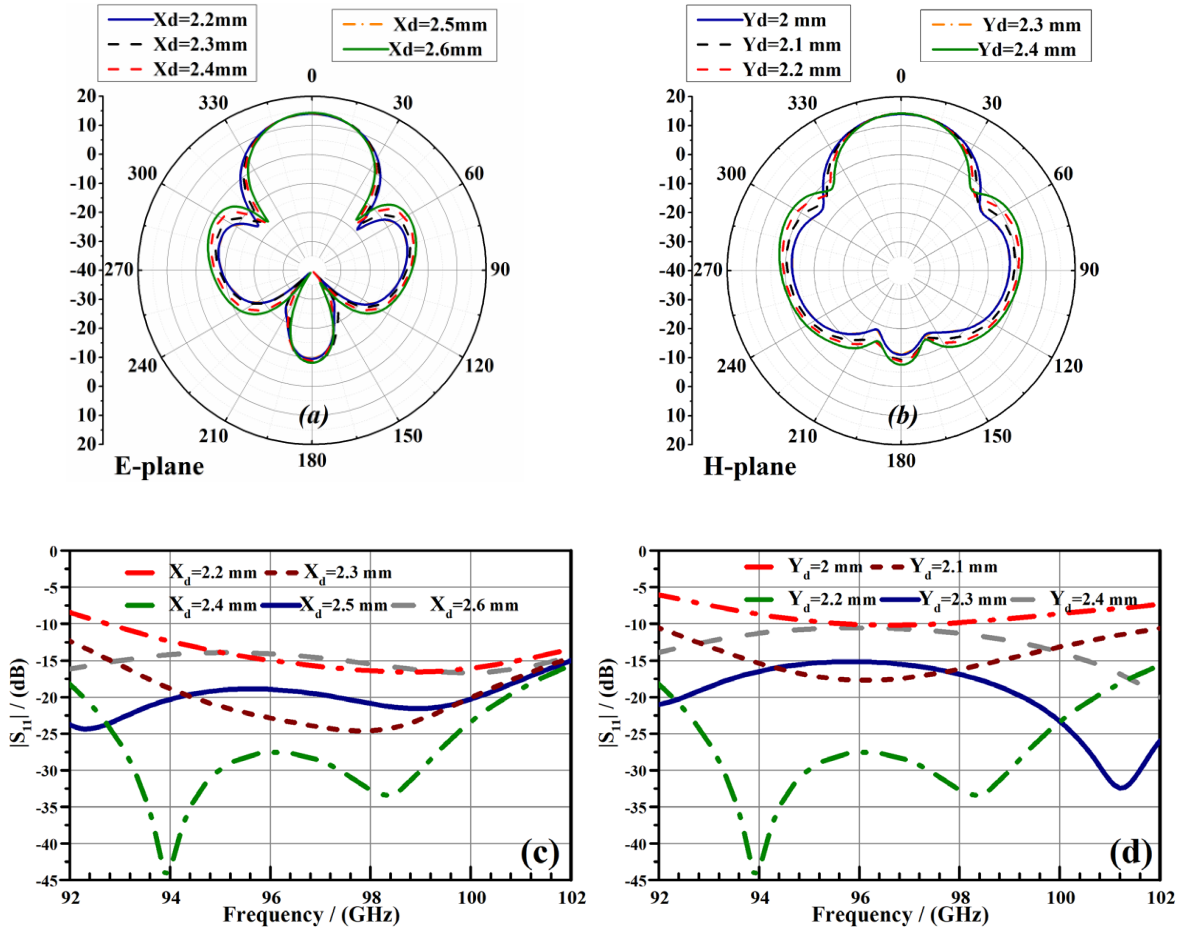

Figure 5. Parameter analysis of the feeding part. (**a**,**b**) Length and width of the cavity. (**c**) Length of the coupling slot. (**d**) Length of the impedance matching step.

Table 1. Dimensions of the proposed 2 × 2-slot sub-array. (Unit: mm).

Parameter	Value	Parameter	Value
a	2.35	w_s	1
b	0.25	h_t	0.25
x_d	2.4	w_c	4.9
l_g	1	y_d	2.2
l_m	1.1	l_c	4.3
w_m	0.92	l_f	2
l_s	1.8	w_f	0.4

2.3. The 4 × 4-Slot Sub-Array Based on Bulk Silicon MEMS Process

Based on the proposed 2 × 2-slot basic unit, a 4 × 4-slot sub-array is built. A one-to-four corporate-feed network, made up of reduced-height RWG H-T dividers, is employed to excite the four 2 × 2-slot basic units. Details of the reduced-height RWG H-T divider are shown in Figure 6. A vertical rectangular transition is designed as the feed port of the 4 × 4-slot sub-array. The geometry of the sub-array is displayed in Figure 7. The spacing between adjacent slots in the x and y directions is 2.9 mm and 2.8 mm, respectively. According to the processing requirements of bulk silicon MEMS technology, the wall thickness of adjacent cavities is greater than 600 µm. The dimensions of the sub-array are 12 mm × 12 mm × 1.25 mm. Figure 8 shows the simulated feeding and radiating performance of the sub-array. The simulated reflection coefficient of the sub-array is greater than 15 dB over the frequency range of 91~97 GHz. The realized gain is greater than 20 dB;

the sidelobe levels are greater than −11.7 dB; and the cross polarization is greater than 40 dB over the operation band. The simulation results indicate that the sub-array has stable radiation characteristics, with a wide working bandwidth, which can be used for larger-scale array design for W-bands.

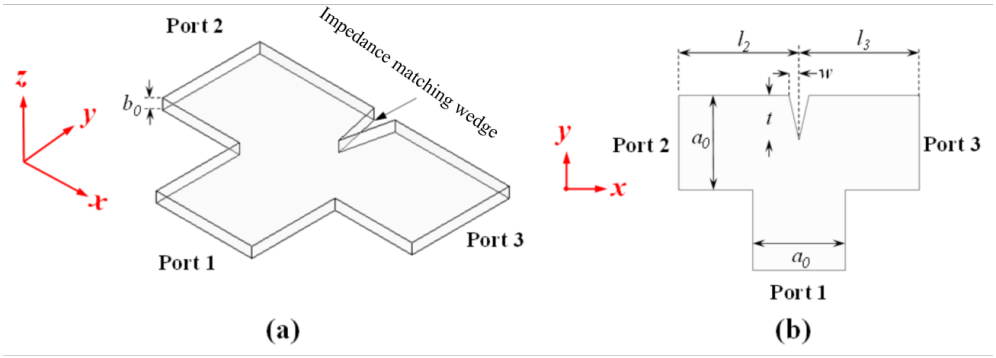

Figure 6. Structure of the reduced-height RWG H-T divider, based on bulk silicon MEMS technology. (**a**) Isometric view. (**b**) Top view.

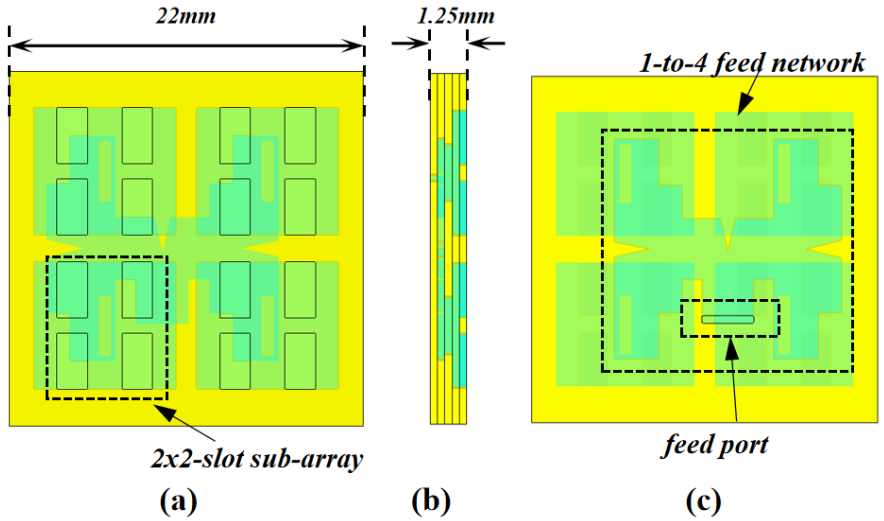

Figure 7. Geometry of the 4 × 4-slot sub-array, based on bulk silicon MEMS technology. (**a**) Front view. (**b**) Side view. (**c**) Back view.

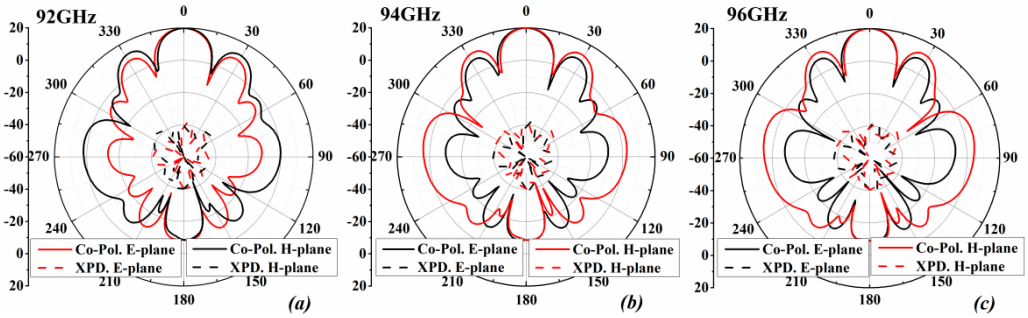

Figure 8. *Cont.*

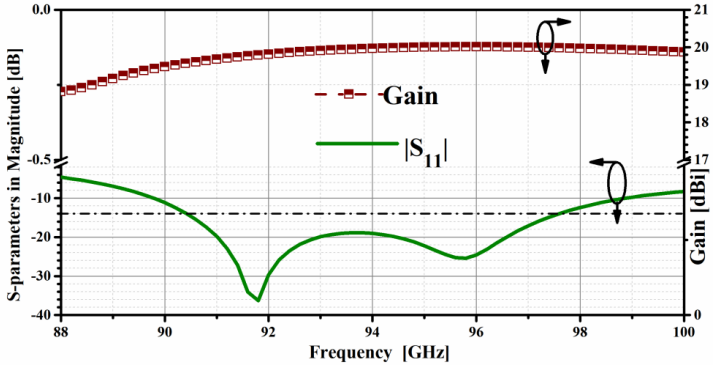

(**d**)

Figure 8. Simulated performances of the 4 × 4-slot sub-array. (**a**–**c**) Radiation patterns. (**d**) S-parameters and gain.

3. The 8 × 8-Slot Hybrid Antenna Array

3.1. Ridge-Gap Waveguide Feed Network

With the increase in array scale, the slot array based on bulk silicon MEMS technology is faced with the problem of fragile structure. Thus, the ridge gap waveguide, which has the features of solid structure, low transmission loss, and easy bonding, is utilized to build the feed network. Based on the 4 × 4-slot sub-array, an 8 × 8-slot hybrid antenna array is designed. The spacings between the adjacent sub-arrays are 13.5 mm ($4.23\lambda_0$) and 12.2 mm ($3.82\lambda_0$) in the x-direction and y-direction, respectively. A one-to-four corporate-feed network, based on RGWG, is designed and simulated to feed the high-gain 8 × 8-slot hybrid antenna array.

The RGWG, H-plane, T-junction power divider and vertical transitions from the RGWG to RWG are employed to construct feed networks. Figure 9 gives the geometry of the RGWG H-T divider and the vertical transitions from the RGWG to RWG. Figure 10 shows the geometry and the simulated performances of the RGWG feed networks. The phase and amplitude differences among all the output ports are within ±10° and ±0.5 dB, and the reflection coefficient of the input ports is less than −15 dB, covering the bandwidth of 90 GHz to 100 GHz.

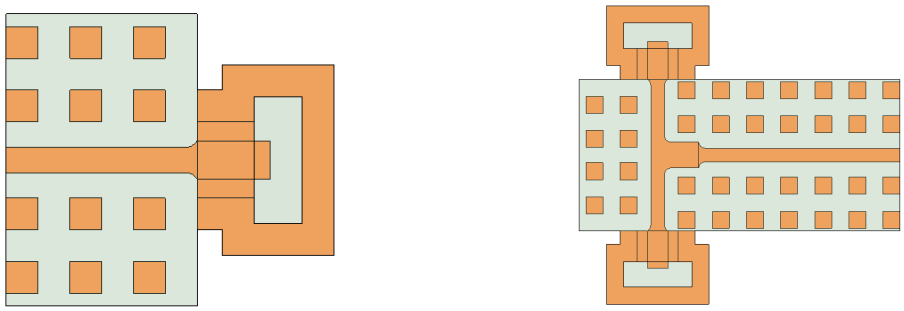

(**a**) (**b**)

Figure 9. *Cont.*

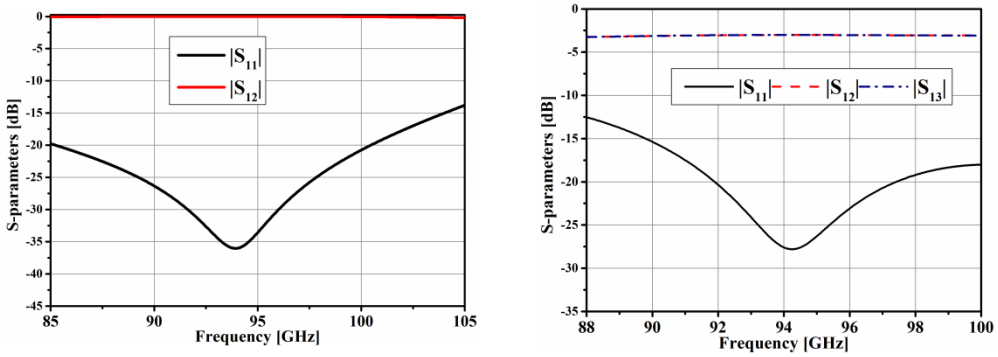

(**c**) (**d**)

Figure 9. The basic unit of the RGWG feed network. (**a**,**c**) Geometry of the vertical transitions from the RGWG to RWG and the simulated S-parameters. (**b**,**d**) Geometry of the RGWG H-T divider and the simulated S-parameters.

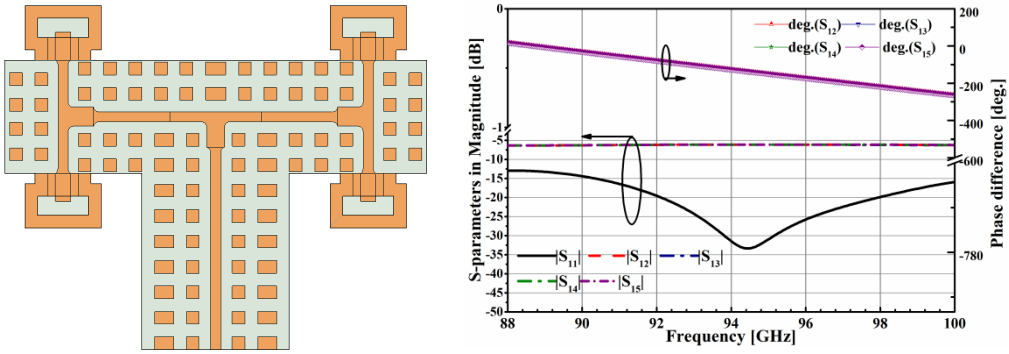

(**a**) (**b**)

Figure 10. Geometry and performance of the RGWG feed network. (**a**) Geometry. (**b**) Simulated performance.

3.2. Fabrication and Measurement

To verify the validity of the proposed antenna array, the simulated 8 × 8-slot hybrid antenna array is fabricated and tested. The four 4 × 4-slot sub-arrays are made up of five silicon wafers, which are etched via the DRIE process and bonded via diffusion bonding under high temperature and pressure. The etching and bonding tolerance of the bulk silicon MEMS process is less than 10 μm.

The RGWG feed network and its cover layer are formed by a silicon–aluminum alloy through a high-precision CNC process. It is worth mentioning that the thermal expansion coefficient silicon–aluminum alloy is closer to silicon than aluminum. To ensure the connection stability between the radiation and feeding part in high- and low-temperature environments, the feed network of the antenna is made up of a silicon–aluminum alloy. The total structure of the hybrid antenna array is shown in Figure 11. The lower surface of the silicon-based sub-array and the upper surface cover plate of the feed network have been plated with gold. The four-waveguide slot sub-array can be integrated with the feed network cover plate, with an accuracy of ±5 μm, by using the low-temperature diffusion bonding process. Then, the integrated cover plate can easily be assembled with the feed network through eight M2 screws, which are uniformly distributed around the cover plate. A WR-10 standard waveguide is located at the central area of the backboard as the feed port. Position accuracy and assembling errors are taken into consideration and analyzed via HFSS.

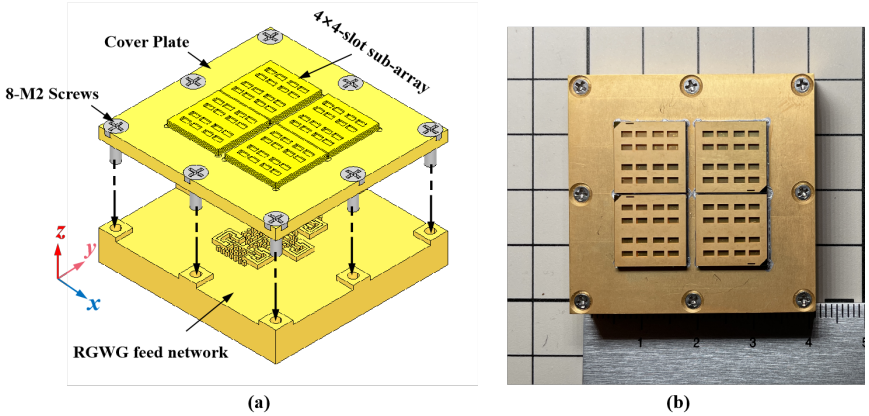

Figure 11. Photograph of the fabricated 8 × 8-slot hybrid antenna array. (**a**) Perspective view. (**b**) Prototype of the hybrid array.

The S-parameter was measured using an R&S Vector Network Analyzer. The radiation performance was evaluated using a near-field antenna measurement system at the W-band. The measurement setup and background are shown in Figure 12. The measured and simulated S-parameters and gains are plotted in Figure 13. The measured results agree well with the simulations. The measured |S11| curves of the antenna array are less than −10 dB over the frequency range of 90.2 GHz to 97.8 GHz with a relative bandwidth of 8.1%. The measured maximum gain of the hybrid array is 26.2 dBi with the radiating efficiency of 65%. The measured gain is lower than the simulated value by 0.4~0.7 dB. The measured gain is 0.3~0.6 dB lower than the simulated value. The difference mainly comes from assembling errors and measurement errors.

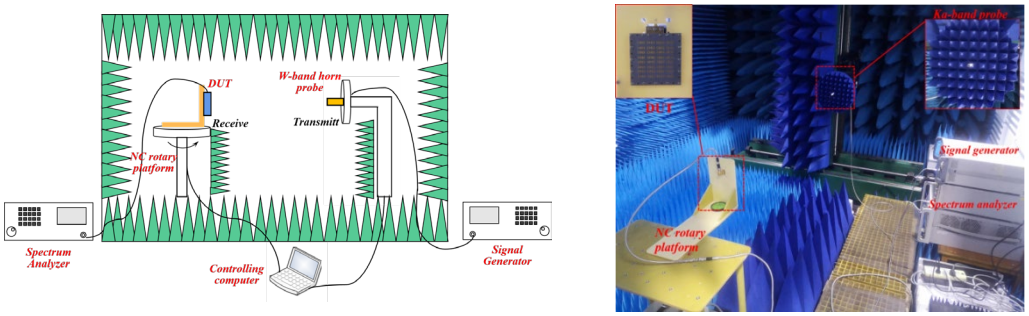

Figure 12. Measurement setup. (**a**) Block diagram of measurement setup. (**b**) Photograph of the measurement setup.

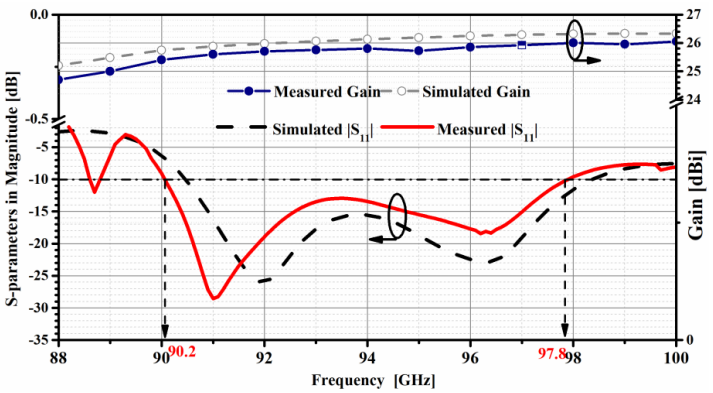

Figure 13. S-parameters and gain of the 8 × 8-slot hybrid antenna array.

The measured radiation patterns in the E-plane and H-plane are shown in Figure 14. The measured first side-lobe levels of the two polarization arrays are less than −11 dB in both the E-plane and the H-plane. The measured and simulated radiation patterns are in good agreement, which verifies the effectiveness of the design.

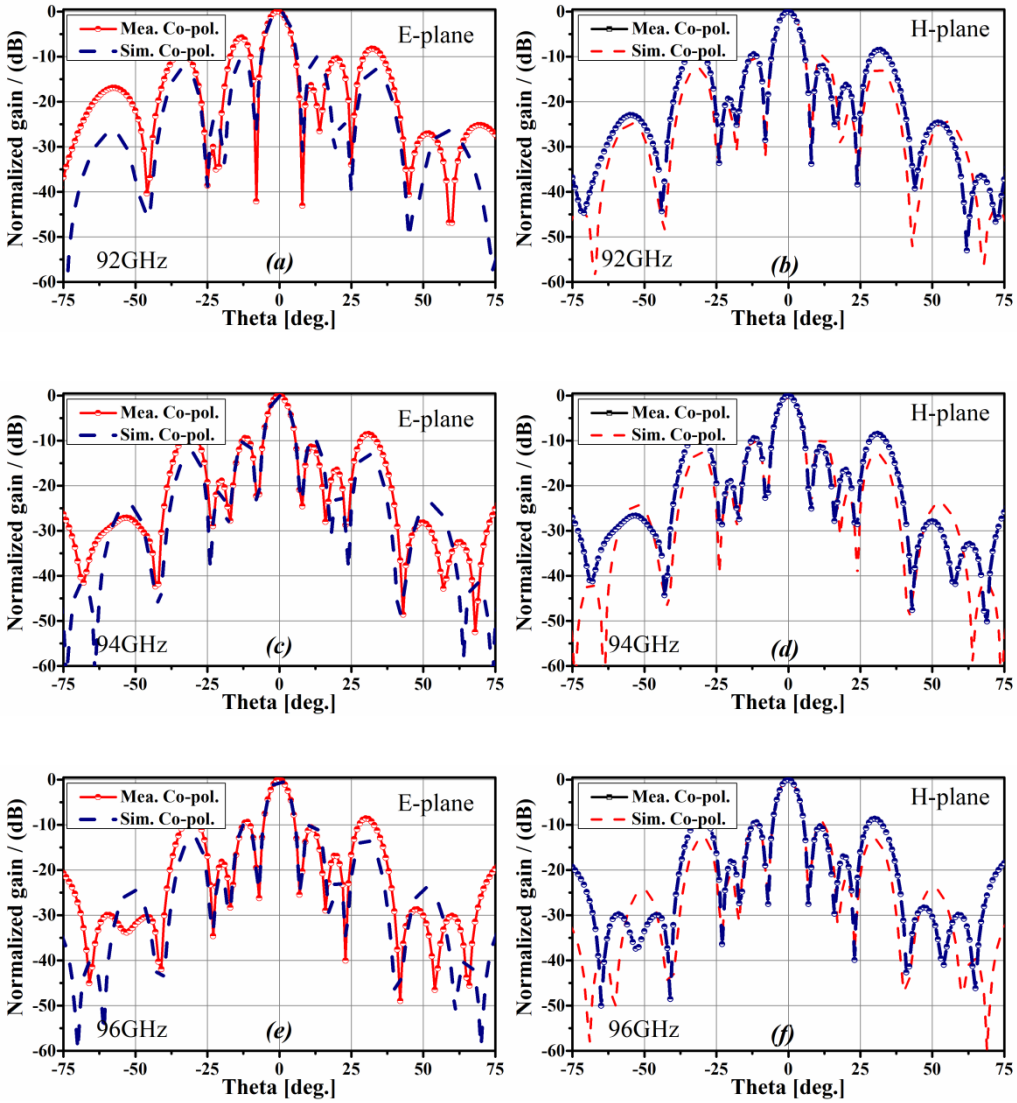

Figure 14. Measured and simulated radiation patterns of the 8 × 8-slot hybrid antenna array. (**a**,**c**,**e**) E-plane, (**b**,**d**,**f**) H-Plane.

Table 2 lists the measured performances of this work with those of the reported planar antenna arrays above 60 GHz. In comparison with the slot antenna array under the electroforming process in [11] and the metal diffusion bonding process in [13], this work has a cheaper fabrication cost. Comparing the planar array between [18] and [22] under multilayer PCB and LTCC processes, respectively, this work shows better radiation efficiency. By comparing the waveguide slot arrays in [24] under the bulk silicon MEMS process, this work also has a wider bandwidth with better fabrication efficiency and cost. In summary, the hybrid slot antenna array proposed in this paper has lower profile and processing costs than those of the slot array, which requires welding technology. On the other hand, the radiation efficiency of this work is higher than that of the antenna array, based on dielectric transmission lines.

Table 2. Performance comparison of the presented mm-wave band planar antenna arrays. (Unit: mm).

Ref.	Fabrication Technology	f_0 (GHz)	B.W($\|S_{11}\|$ < −10 dB)	Num. Of Unit	SLL (dB)	Max. Gain (dBi)	Max Rad. Efficiency	Fabrication Efficiency	Fabrication Cost
[11]	Electroforming	94	8.3%	8 × 8	−8	26.8	81.9%	Low	High
[13]	Laser etching + Diffusion bonding	60	10.9%	16 ×16	−11	32	80%	High	High
[18]	Multilayer PCB	63	14.6%	32 × 32	−10	39.2	51%	High	Low
[22]	LTCC + Metal CNC	94	14.9%	8 × 8	−11	23.8	42%	High	Moderate
[24]	Bulk silicon MEMS	59	2.2%	1 × 8	−18.6	13.3	45%	High	High
This work	Bulk silicon MEMS + Metal CNC	94	8.1%	8 × 8	−11	26.2	65.2%	High	Moderate

4. Conclusions

A W-band, high-gain, hybrid slot antenna array is proposed. It uses the high-order-mode excited cavity slot processed using bulk silicon MEMS technology as the radiation unit, and the feed network is constructed by the RGWG of the unclosed structure. The measured results show that the slot array antenna, excited by high-order TM_{240} mode, can achieve an 8.1% ($|S_{11}| < -10$ dB) impedance bandwidth, covering from 91.2 to 97.27 GHz, with a maximum gain of 26.2 dBi over the operating band. The measured first side-lobe level is less than −11 dB. With good feeding and radiating performance, high fabrication efficiency, and moderate fabrication cost, the hybrid slot antenna array proposed in this work exhibits potential usage in W-band radars and wireless systems.

Author Contributions: Conceptualization, Y.Z. and H.L.; methodology, W.T. and Y.Z.; software, W.T. and Z.Z.; validation, Z.Z. and W.T.; formal analysis, H.L. and Y.Z.; investigation, W.T.; resources, Y.Z.; data curation, Y.Z. and W.T.; writing—original draft preparation, Y.Z.; writing—review and editing, H.L. and G.Z.; visualization, H.L. and W.T.; supervision, H.S.; project administration, Y.Z.; funding acquisition, Y.Z. All authors have read and agreed to the published version of the manuscript.

Funding: This research was supported by Beijing Key Laboratory of Millimeter Wave and Terahertz Techniques.

Conflicts of Interest: The authors declare no conflict of interest.

References

1. Xu, J.; Hong, W.; Zhang, H.; Wang, G.; Yu, Y.; Jiang, Z.H. An Array Antenna for Both Long- and Medium-Range 77 GHz Automotive Radar Applications. *IEEE Trans. Antennas Propag.* **2017**, *65*, 7207–7216. [CrossRef]
2. Teng, X.; Luo, Y.; Yan, N.; Ma, K. A Cavity-Backed Antenna Using SISL Technology for 77 GHz Band Application. *IEEE Trans. Antennas Propag.* **2022**, *70*, 3840–3845. [CrossRef]
3. Wu, B.; He, L. Multilayered Circular Dielectric Structure SAR Imaging Based on Compressed Sensing for FOD Detection in NDT. *IEEE Trans. Instrum. Meas.* **2020**, *69*, 7588–7593. [CrossRef]
4. Shi, Q.; Wu, J.; Ni, Z.; Lv, X.; Ye, F.; Hou, Q.; Chen, X. A Blast Furnace Burden Surface Deeplearning Detection System Based on Radar Spectrum Restructured by Entropy Weight. *IEEE Sens. J.* **2021**, *21*, 7928–7939. [CrossRef]
5. Tong, X.; Jiang, Z.H.; Yu, C.; Wu, F.; Xu, X.; Hong, W. Low-Profile, Broadband, Dual-Linearly Polarized, and Wide-Angle Millimeter-Wave Antenna Arrays for Ka-Band 5G Applications. *IEEE Antennas Wirel. Propag. Lett.* **2021**, *20*, 2038–2042. [CrossRef]
6. Shen, X.; Liu, Y.; Zhao, L.; Huang, G.-L.; Shi, X.; Huang, Q. A Miniaturized Microstrip Antenna Array at 5G Millimeter-Wave Band. *IEEE Antennas Wirel. Propag. Lett.* **2019**, *18*, 1671–1675. [CrossRef]
7. Yang, T.Y.; Hong, W.; Zhang, Y. Wideband Millimeter-Wave Substrate Integrated Waveguide Cavity-Backed Rectangular Patch Antenna. *IEEE Antennas Wirel. Propag. Lett.* **2014**, *13*, 205–208. [CrossRef]
8. Lu, J.; Zhang, H.; Wang, W.; Liang, X.; Ge, J.; Jin, M.; Wu, W. Broadband Dual-Polarized Waveguide Slot Filtenna Array with Low Cross Polarization and High Efficiency. *IEEE Trans. Antennas Propag.* **2019**, *67*, 151–159. [CrossRef]
9. Li, T.; Meng, H.; Dou, W. Design and Implementation of Dual-Frequency Dual-Polarization Slotted Waveguide Antenna Array for Ka-Band Application. *IEEE Antennas Wirel. Propag. Lett.* **2014**, *13*, 1317–1320.
10. Chen, M.; Fang, X.-C.; Wang, W.; Zhang, H.-T.; Huang, G.-L. Dual-Band Dual-Polarized Waveguide Slot Antenna for SAR Applications. *IEEE Antennas Wirel. Propag. Lett.* **2020**, *19*, 1719–1723. [CrossRef]
11. Kim, D.-Y.; Lim, Y.; Yoon, H.-S.; Nam, S. High-Efficiency W-Band Electroforming Slot Array Antenna. *IEEE Trans. Antennas Propag.* **2015**, *63*, 1854–1857. [CrossRef]
12. Kim, D.; Zhang, M.; Hirokawa, J.; Ando, M. Design and Fabrication of a Dual-Polarization Waveguide Slot Array Antenna with High Isolation and High Antenna Efficiency for the 60 GHz Band. *IEEE Trans. Antennas Propag.* **2014**, *62*, 3019–3027. [CrossRef]

13. Tomura, T.; Hirokawa, J.; Hirano, T.; Ando, M. A 45° Linearly Polarized Hollow-Waveguide 16 × 16-Slot Array Antenna Covering 71–86 GHz Band. *IEEE Trans. Antennas Propag.* **2014**, *62*, 5061–5067. [CrossRef]
14. Sano, M.; Hirokawa, J.; Ando, M. Single-Layer Corporate-Feed Slot Array in the 60-GHz Band Using Hollow Rectangular Coaxial Lines. *IEEE Trans. Antennas Propag.* **2014**, *62*, 5068–5076. [CrossRef]
15. Kim, D.; Hirokawa, J.; Ando, M.; Takeuchi, J.; Hirata, A. 64× 64-Element and 32× 32-Element Slot Array Antennas Using Double-Layer Hollow-Waveguide Corporate-Feed in the 120 GHz Band. *IEEE Trans. Antennas Propag.* **2014**, *62*, 1507–1512. [CrossRef]
16. Cheng, Y.J.; Guo, Y.X.; Liu, Z.G. W-Band Large-Scale High-Gain Planar Integrated Antenna Array. *IEEE Trans. Antennas Propag.* **2014**, *62*, 3370–3373. [CrossRef]
17. Chen, X.-P.; Wu, K.; Han, L.; He, F. Low-Cost High Gain Planar Antenna Array for 60-GHz Band Applications. *IEEE Trans. Antennas Propag.* **2010**, *58*, 2126–2129. [CrossRef]
18. Wu, J.; Cheng, Y.J.; Fan, Y. A Wideband High-Gain High-Efficiency Hybrid Integrated Plate Array Antenna for V-Band Inter-Satellite Links. *IEEE Trans. Antennas Propag.* **2015**, *63*, 1225–1233. [CrossRef]
19. Ferrando-Rocher, M.; Herranz-Herruzo, J.I.; Valero-Nogueira, A.; Bernardo-Clemente, B.; Herranz, J.I.; Bernardo, B. Full-Metal K-Ka Dual-Band Shared-Aperture Array Antenna Fed by Combined Ridge-Groove Gap Waveguide. *IEEE Antennas Wirel. Propag. Lett.* **2019**, *18*, 1463–1467. [CrossRef]
20. Ferrando-Rocher, M.; Herranz-Herruzo, J.I.; Valero-Nogueira, A.; Vila-Jimenez, A. Single-Layer Circularly-Polarized Ka-Band Antenna Using Gap Waveguide Technology. *IEEE Trans. Antennas Propag.* **2018**, *66*, 3837–3845. [CrossRef]
21. Cao, B.; Shi, Y.; Feng, W. W-Band LTCC Circularly Polarized Antenna Array with Mixed U-Type Substrate Integrated Waveguide and Ridge Gap Waveguide Feeding Networks. *IEEE Antennas Wirel. Propag. Lett.* **2019**, *18*, 2399–2403. [CrossRef]
22. Cao, B.; Wang, H.; Huang, Y.; Zheng, J. High-Gain L-Probe Excited Substrate Integrated Cavity Antenna Array with LTCC-Based Gap Waveguide Feeding Network for W-Band Application. *IEEE Trans. Antennas Propag.* **2015**, *63*, 5465–5474. [CrossRef]
23. Cao, J.; Wang, H.; Mou, S.; Soothar, P.; Zhou, J. An Air Cavity-Fed Circularly Polarized Magneto-Electric Dipole Antenna Array with Gap Waveguide Technology for mm-Wave Applications. *IEEE Trans. Antennas Propag.* **2019**, *67*, 6211–6216. [CrossRef]
24. Chang, L.; Li, Y.; Zhang, Z.J.; Feng, Z.H. Low-Sidelobe Air-Filled Slot Array Fabricated Using Silicon Micromachining Technology for Millimeter-Wave Application. *IEEE Trans. Antennas Propag.* **2017**, *65*, 4067–4074. [CrossRef]
25. Cheng, Y.J.; Tan, F.Y.; Zhou, M.M.; Fan, Y. Dual-Polarized Wideband Plate Array Antenna with High Polarization Isolation and Low Cross Polarization for D-Band High-Capacity Wireless Application. *IEEE Trans. Antennas Propag.* **2020**, *19*, 2023–2027. [CrossRef]
26. Yao, S.S.; Cheng, Y.J.; Wu, Y.; Fan, Y. Isolation Enhancement for W-Band Coplanar Array Antennas Based on Silicon Micromachining Technology. *IEEE Antennas Wirel. Propag. Lett.* **2020**, *19*, 1744–1748. [CrossRef]